Applied Surface Science 618 (2023) 156652

Contents lists available at ScienceDirect

Applied Surface Science

journal homepage: www.elsevier.com/locate/apsusc

Full Length Article

Functionalization of graphitic carbon nitride systems by cobalt and cobalt-iron oxides boosts solar water oxidation performances

Mattia Benedet [a], Gian Andrea Rizzi [a,b,*], Alberto Gasparotto [a,b], Nicolas Gauquelin [c], Andrey Orekhov [c], Johan Verbeeck [c], Chiara Maccato [a,b,*], Davide Barreca [b]

[a] Department of Chemical Sciences, Padova University and INSTM, 35131 Padova, Italy
[b] CNR-ICMATE and INSTM, Department of Chemical Sciences, Padova University, 35131 Padova, Italy
[c] EMAT and NANOlab Center of Excellence, University of Antwerp, 2020 Antwerpen, Belgium

ARTICLE INFO

Keywords:
CoO
$CoFe_2O_4$
Graphitic carbon nitride
RF-sputtering
Oxygen evolution reaction

ABSTRACT

The ever-increasing energy demand from the world population has made the intensive use of fossil fuels an overarching threat to global environment and human health. An appealing alternative is offered by sunlight-assisted photoelectrochemical water splitting to yield carbon-free hydrogen fuel, but kinetic limitations associated to the oxygen evolution reaction (OER) render the development of cost-effective, eco-friendly and stable electrocatalysts an imperative issue. In the present work, OER catalysts based on graphitic carbon nitride (g-C_3N_4) were deposited on conducting glass substrates by a simple decantation procedure, followed by functionalization with low amounts of nanostructured CoO and $CoFe_2O_4$ by radio frequency (RF)-sputtering, and final annealing under inert atmosphere. A combination of advanced characterization tools was used to investigate the interplay between material features and electrochemical performances. The obtained results highlighted the formation of a *p-n* junction for the g-C_3N_4-CoO system, whereas a *Z*-scheme junction accounted for the remarkable performance enhancement yielded by g-C_3N_4-$CoFe_2O_4$. The intimate contact between the system components also afforded an improved electrocatalyst stability in comparison to various bare and functionalized g-C_3N_4-based systems. These findings emphasize the importance of tailoring g-C_3N_4 chemico-physical properties through the dispersion of complementary catalysts to fully exploit its applicative potential.

1. Introduction

The ever-increasing overreliance on the burning of non-renewable fossil fuels and the consequent detrimental greenhouse gases emission have stimulated the exploration of green energy alternatives to suppress global warming and environmental pollution [1–2]. In this context, an urgent need highlighted by the Intergovernmental Panel on Climate Change (IPCC) is to decarbonize the current energy portfolio to a cleaner and more sustainable one [3–4], as promised by the transition to a hydrogen-based economy. In fact, molecular hydrogen (H_2) stands as an attractive energy vector thanks to its high energy density (≈142 MJ × kg^{-1}) and carbon-free nature [5–6]. The abundant sunlight, a renewable and inexhaustible natural resource reaching the Earth surface (1.3×10^5 TW per year), provides a valuable means for a sustainable production of H_2, which, to date, is mainly obtained on an industrial scale by energy-intensive steam reforming [7]. In particular, photoeletrochemical water splitting into O_2 and H_2 features a remarkable applicative potential towards a clean and large-scale hydrogen generation [8–10]. Nonetheless, the overall process efficiency is limited by the kinetic limitations associated to the oxygen evolution reaction (OER) [8,10–12], the bottleneck of water splitting. To date, noble metal oxides (IrO_2 and RuO_2) are regarded as the OER benchmark catalysts, but their large-scale application is precluded by their high cost, environmental footprint and supply shortage [11,13–14]. As a consequence, the development and implementation of cost-effective, highly active and stable OER catalysts based on earth-abundant and eco-friendly elements is highly demanded for a commercially viable H_2 generation without any significant harm on environment and human health.

In the actual tide of possible candidates, graphitic carbon nitride (g-C_3N_4), a cost-effective and metal-free semiconductor, presents a range of superior properties if compared to other possible systems. These include its high thermal and physico-chemical stability in basic/acidic media, amenable reactivity, suitable band edges for water splitting, tuneable electronic structure, and band gap enabling Vis light harvesting (E_G ≈

* Corresponding authors at: Department of Chemical Sciences, Padova University and INSTM, 35131 Padova, Italy.
E-mail addresses: gianandrea.rizzi@unipd.it (G. Andrea Rizzi), chiara.maccato@unipd.it (C. Maccato).

https://doi.org/10.1016/j.apsusc.2023.156652
Received 15 November 2022; Received in revised form 27 January 2023; Accepted 1 February 2023
Available online 4 February 2023

2.7 eV) [1,15–22]. It is worthwhile highlighting that g-C_3N_4 consists of earth-abundant and non-toxic elements, a feature rendering it a very attractive alternative for real-world applications in comparison to widely used metal oxide-containing OER electrocatalysts, to reduce the environmental footprint and improve the process sustainability. As a consequence, over the last decade g-C_3N_4 systems have been the subject of a huge number of research works worldwide. Nevertheless, the above mentioned advantages are partially eclipsed by the low active area, limited amount of active sites, and relatively rapid electron-hole recombination [23–24]. To this regard, two successful strategies to enhance bare g-C_3N_4 activity are based on the tailoring of its nano-organization and on its combination with transition metal oxide complementary catalysts [15,25–27]. The latter option is, in principle, highly appealing not only to improve g-C_3N_4 absorption, but also to enhance charge carrier separation through the construction of suitable semiconductor heterojunctions. A careful choice of the system components and the implementation of versatile preparation routes, which, in turn, directly influence the nature of the established material junctions [28], open broad perspectives to modulate and boost functional performances in view of possible large-scale end-uses [16,26,29].

In this work, we present an amenable and innovative fabrication route to supported OER photoelectrocatalysts based on the combination of g-C_3N_4 with single and multi-metal transition metal oxide nanoparticles. In particular, CoO and $CoFe_2O_4$ have been chosen as functional activators due to their inherent catalytic activity in different oxidation reactions, enabling an improvement of bare g-C_3N_4 behavior in various photo-assisted processes, including water oxidation [18,29–31]. Up to date, composite systems combining g-C_3N_4 with CoO and $CoFe_2O_4$ have been mainly prepared by wet synthetic procedures for electrochemical supercapacitors [32] and photocatalysts for pollutant degradation [17–18,33–36], and some studies have focused on their use in H_2O splitting [16,30,37]. To the best of our knowledge, so far the target materials have been mainly investigated in a powdered form [16–18,21,33–36], whereas only few contributions have been dedicated to supported systems [30,32,37–38], which are highly required for a practical integration in real-world end-uses.

Herein, g-C_3N_4 deposits were prepared on conductive glass substrates by a simple and cost-effective decantation procedure, involving the use of pre-synthesized powders obtained by thermal condensation of melamine. Subsequently, g-C_3N_4 deposits were functionalized with ultra-dispersed CoO and $CoFe_2O_4$ nanoparticles *via* radio frequency (RF)-sputtering from non-equilibrium plasmas (see Fig. 1). The main advantages of the adopted preparation route, which, to our knowledge, has never been employed before for the preparation of the target materials, are related to the inherent sputtering infiltration power and the possibility of achieving a controlled g-C_3N_4 functionalization under mild operational conditions. The resulting intimate contact between the system components is of key importance in order to favorably exploit their mutual chemical/electronic interactions, ultimately leading to enhanced functional performances. In particular, the functionalization

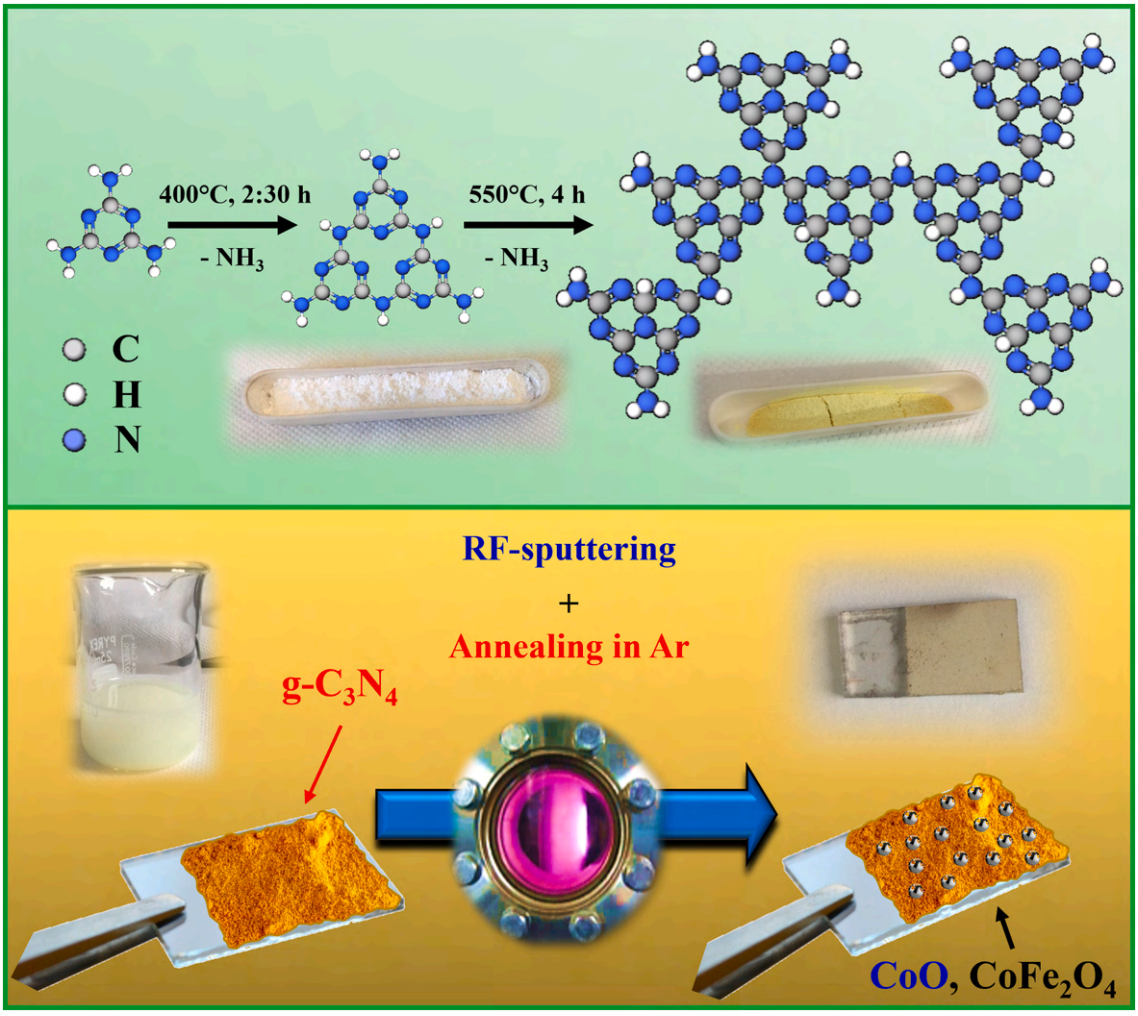

Fig. 1. Sketch of the fabrication procedure adopted in the present work for carbon nitride (g-C_3N_4)-based electrodes functionalized with CoO (g-C_3N_4-CoO) and $CoFe_2O_4$ (g-C_3N_4-$CoFe_2O_4$).

of g-C_3N_4 with CoO [16,23,29,35,39], and especially with $CoFe_2O_4$ [17–18,33,38], resulted in the tailored formation of carbon nitride/metal oxide heterojunctions. Photoelectrochemical tests enabled to attain a valuable insight into the nature of these junctions (CoO/g-C_3N_4 or $CoFe_2O_4$/g-C_3N_4) and their efficiency in the Vis light-production of electron/hole pairs, with particular regard to the enhancement of hole concentration on oxide nanoparticles in contact with the reaction medium. As a result, the target systems, and especially g-C_3N_4-$CoFe_2O_4$, featured an attractive photoactivity increase in comparison to the pristine g-C_3N_4 in the proximity of H_2O thermodynamic oxidation potential. In addition, the developed materials yielded a favorable operational stability in comparison to various g-C_3N_4-based electrocatalysts, an important figure of merit for real-world end-uses. In this study, the origins of performance boosting brought about by g-C_3N_4 functionalization are presented and critically discussed basing on the outcomes of a multi-technique characterization, which enabled to elucidate the interplay between material structure, composition, nano-organization and photoelectrochemical performances. The obtained results may act as a useful guide for further implementation of highly active, economically viable and stable OER photoanodes aimed at solar hydrogen production.

2. Experimental section

2.1. Material synthesis

The deposition of g-C_3N_4 on fluorine-doped tin oxide (FTO)-coated glass substrates was accomplished by a decantation procedure. In particular, pre-grinded carbon nitride powders (16 mg), synthesized as reported in the Supporting Information (SI; see also Fig. S1) were preliminarily suspended in 8 mL isopropanol and sonicated for 1 h. The suspension was transferred into a beaker, in which a suitably pre-cleaned FTO glass slide (Aldrich®; ≈7 Ω × sq^{-1}; FTO layer thickness ≈600 nm) was laid on the bottom for 24 h. The resulting deposit was dried in air for 15 min before undergoing annealing in an Ar atmosphere (500 °C for 2.5 h; heating rate = 3 °C/min).

g-C_3N_4 functionalization was performed by RF-sputtering from weakly ionized Ar plasmas (purity = 5.0), using a two-electrode custom-built plasmochemical reactor (ν = 13.56 MHz). Co (Alfa Aesar®; thickness = 0.25 mm; purity = 99.95 %; diameter = 5 cm) or Co_3O_4-Fe_2O_3 targets (Neyco; thickness = 2 mm; purity = 99.9 %; 50 × 50 mm^2) were fixed on the RF-electrode, whereas FTO-supported g-C_3N_4 specimens were mounted on the grounded one. Hereafter, the obtained functionalized systems are indicated as g-C_3N_4-A, where A = CoO or $CoFe_2O_4$. Basing on previous results [40], depositions were performed using the following optimized experimental settings: RF-power = 20 W; growth temperature = 60 °C; Ar flow rate = 10 standard cubic centimeters per minute (sccm); total pressure = 0.3 mbar; process duration = 180 and 195 min for g-C_3N_4-CoO and g-C_3N_4-$CoFe_2O_4$, respectively. All the resulting materials were finally annealed in Ar atmospheres (500 °C, 2.5 h; heating rate = 3 °C/min).

2.2. Material characterization

X-ray photoelectron (XPS) analyses were carried out on a Perkin-Elmer Φ 5600-ci instrument at a pressure < 10^{-8} mbar using a non-monochromatized Mg Kα excitation ($h\nu$ = 1253.6 eV), to avoid the overlap of Co and Fe Auger peaks with Fe2p and Co2p ones, respectively, occurring with the standard Al Kα X-ray source [10]. No sputtering was carried out. Binding energy (BE) values were corrected for charging effects by assigning a value of 284.8 eV to the adventitious C1s signal [41]. After a Shirley-type background subtraction, peak fitting was carried out by the XPSPEAK software (accessed June 2022 [42]). Atomic percentages (at. %) were calculated by peak area integration using Φ V5.4A sensitivity factors. Field emission-scanning electron microscopy (FE-SEM) analyses were performed using a Zeiss SUPRA 40VP instrument, at primary beam acceleration voltages of 10–20 kV. Selected area electron diffraction (SAED) and energy dispersive X-ray spectroscopy (EDXS) analyses were carried out on a ThermoFisher Scientific Osiris microscope equipped with a Super-X windowless EDX detector system operated at 200 kV. High-resolution electron energy loss spectroscopy (EELS) data were recorded using a state-of-the-art double-corrected and monochromated Thermo Fisher Scientific Titan^3 80–300 microscope operated at 120 kV (energy resolution = 120 meV; convergence and collection angle = 19 and 90 mrad, respectively). Spectra were acquired on a Direct detection Gatan K2 camera mounted on a GIF Quantum spectrometer (0.2 s/pixel). Reference spectra on CoO and Co_3O_4 were acquired with a dispersion of 0.1 eV/pixel, whereas spectra for g-C_3N_4–CoO and g-C_3N_4-$CoFe_2O_4$ were acquired with a dispersion of 0.05 eV/pixel. Energy calibration issues were corrected by aligning the experimental spectrum to the reference one, and the dispersion of the g-C_3N_4–CoO and g-C_3N_4-$CoFe_2O_4$ spectra was found to be 0.0505 eV/pixel. High-resolution scanning transmission electron microscopy (STEM) images were acquired at 300 kV acceleration voltage using 50 pA probe current, a convergence semi-angle of 21 mrad, and collection angles of 29-160 mrad [high angle annular dark field (HAADF) imaging] and 0–20 mrad [bright field (BF) imaging]. Optical absorption spectra were registered operating in diffuse reflectance mode by a Cary 50 (Varian) dual-beam spectrophotometer (spectral bandwidth = 1 nm). Band gap (E_G) evaluation was performed using the Tauc equation $[f(R)\ h\nu]^n$ *vs* $h\nu$, where f(R) is the Kubelka-Munk function and R is the measured reflectance, assuming the occurrence of allowed indirect transitions (n = ½) [12,18,39].

2.3. Photoelectrochemical tests

Photoelectrochemical measurements were carried out at room temperature using an electrochemical working station (Autolab PGSTAT204 potentiostat/galvanostat) and a three-electrode set-up. The FTO-supported materials were employed as working electrodes (WEs), while a Pt coil was used as counterelectrode (CE). A standard calomel electrode (SCE) was employed as reference electrode (RE). Prior to measurements, samples were cycled between 1.0 and 1.8 V *vs* the reversible hydrogen electrode (RHE), until a constant behavior was obtained. During a typical test, the WE was illuminated on the front side (electrode–electrolyte interface) using a white light LED source. A 0.1 M KOH solution (pH = 12.9) was used as the electrolyte. The potential *vs* SCE (E_{SCE}) was converted into the RHE scale using the formula:

$$E_{RHE} = E_{WE}(V) + E_{SCE}(V) + 0.0592 \cdot pH \quad (1)$$

where E_{WE} represents the bias applied to the working electrode. Linear sweep voltammetry (LSV) curves were collected at a scan rate of 5 mV s^{-1}. Current density (j) values were obtained by normalizing the measured currents for the exposed geometric area (0.283 cm^2). Chronoamperometry (CA) analyses were performed at 1.5 V *vs* RHE.

Applied bias photon-to-current efficiency (ABPE) curves were derived from photocurrent density *vs* bias data through the following equation [43]:

$$ABPE\ (\%) = ([j \times (1.23 - E_{RHE})]/P) \times 100 \quad (2)$$

where j (mA × cm^{-2}) is the photocurrent density at a given applied potential (E_{RHE}) and P is the incident light intensity (≈150 mW × cm^{-2}).

Further details on material synthesis and characterization are reported in the SI.

3. Results and discussion

3.1. Material characterization

The surface chemical composition was investigated by XPS, a fundamental analytical tool to investigate the elemental chemical environments in g-C_3N_4-based materials [44]. Wide-scan spectra (Fig. S2)

revealed the presence of C and N photopeaks, as expected. For functionalized specimens, even the occurrence of cobalt (g-C_3N_4-CoO), or cobalt and iron (g-C_3N_4-$CoFe_2O_4$) photoelectron and Auger signals could be clearly discerned, suggesting a dispersion of functionalizing agents over the underlying carbon nitride, with no complete coverage of the latter.

Quantitative analyses (Table S1) indicated an increase in the oxygen content upon going from bare carbon nitride (g-C_3N_4) to functionalized specimens (g-C_3N_4-CoO and g-C_3N_4-$CoFe_2O_4$), pointing out the occurrence of Co and Fe in oxidized forms. The average N/C at.% ratio of (1.20 ± 0.08) (see Table S1), slightly lower than the value for stoichiometric g-C_3N_4 (1.33), suggested the presence of nitrogen deficiencies. The latter, whose role in carbon nitride-based photocatalysts is rarely considered, can play a key role in modifying photoactivated material performances [45]. In order to achieve a deeper insight into the elemental chemical environments, narrow scan C1s and N1s photopeaks were recorded and deconvoluted. As can be observed in Fig. 2a and S3 (compare also Table S2), irrespective of the specific sample, three different components contributed to the overall C1s signal (see Fig. 2c for a detailed assignment): **i**) adventitious carbon contamination (BE = 284.8 eV) [46–48]; **ii**) carbon bonded to amino groups (C-NH_x, x = 1, 2) on g-C_3N_4 heptazine ring edges (average BE = 286.2 eV) [12,49]; **iii**), the predominant contribution, due to *N*-C═N carbon atoms in the aromatic rings of g-C_3N_4 framework (mean BE = 288.3 eV) [16,35,39,46,50]. At variance with previous studies [48], no appreciable bands related to C—O moieties could be observed.

For all samples, the N1s signal could be deconvoluted by means of the following four bands (Fig. 2b and S3; see also Fig. 2c): **iv**), the main one (average BE = 398.6 eV), attributable to bi-coordinated nitrogen centers (C═N-C) [51–54]; **v**), with an average BE of 399.8 eV, ascribed to tri-coordinated N atoms [N-$(C)_3$] in the g-C_3N_4 structure [44,46,49–50,52]; **vi**), related to NH_x (x = 1, 2) groups in the heptazine framework (average BE = 401.0 eV) [44,47–48,50,53,55]; **vii**), due to π-electrons excitations in heptazine rings (mean BE = 404.2 eV) [16,39,47,52]. The contribution of component (**vi**) to the N1s signal (Fig. 2d and Table S3) increased according to the following sequence: g-C_3N_4 < g-C_3N_4-CoO < g-C_3N_4-$CoFe_2O_4$, suggesting a parallel enhancement of defects resulting from -NH_x presence, due, in turn, to carbon nitride bombardment during RF-sputtering. Such defects can act as capturing sites, minimizing charge carrier recombination and enhancing thus the system photoactivity [49,56]. Details on the O1s spectral features are reported in the SI (see Fig. S4, Table S4 and related comments).

The analysis of Co and Fe oxidation states in the target materials required particular attention. For both g-C_3N_4-CoO and g-C_3N_4-$CoFe_2O_4$ samples, the Co2p photopeak (Fig. 2e) had a qualitatively similar band shape and was characterized by intense shake-up satellites at BEs ≈ 5.1 eV higher than the corresponding spin–orbit components. This indication was a clear fingerprint for the occurrence of high-spin Co(II) centers at the system surface [29–31,39,41,57]. For sample g-C_3N_4-CoO, the signal energy location [BE($Co2p_{3/2}$) = 781.1 eV; spin–orbit splitting (SOS) separation = 15.7 eV] was in excellent agreement with the presence of CoO [16,18,34–35,39], with no other cobalt oxides in appreciable amounts. As a matter of fact, CoO occurrence can be deemed to be promising for the present applications, taking into account that nanocrystalline cobalt(II) oxide, differently from the corresponding bulk phase, possesses a very favorable activity as solar water splitting photocatalyst [29]. The lack of signals centered at 778.0–779.0 eV pointed out the absence of Co metal impurities [39].

As far as specimen g-C_3N_4-$CoFe_2O_4$ is concerned, the Co2p position underwent an upward shift of + 0.2 eV with respect to g-C_3N_4-CoO. The obtained value [BE($Co2p_{3/2}$) = 781.3 eV; see Fig. 2e] was compatible with that previously reported for Co centers in $CoFe_2O_4$-containing systems [33,55,58–59]. The Fe2p peak, free from evident shake-up satellites on the high BE sides of the main spin–orbit components [BE

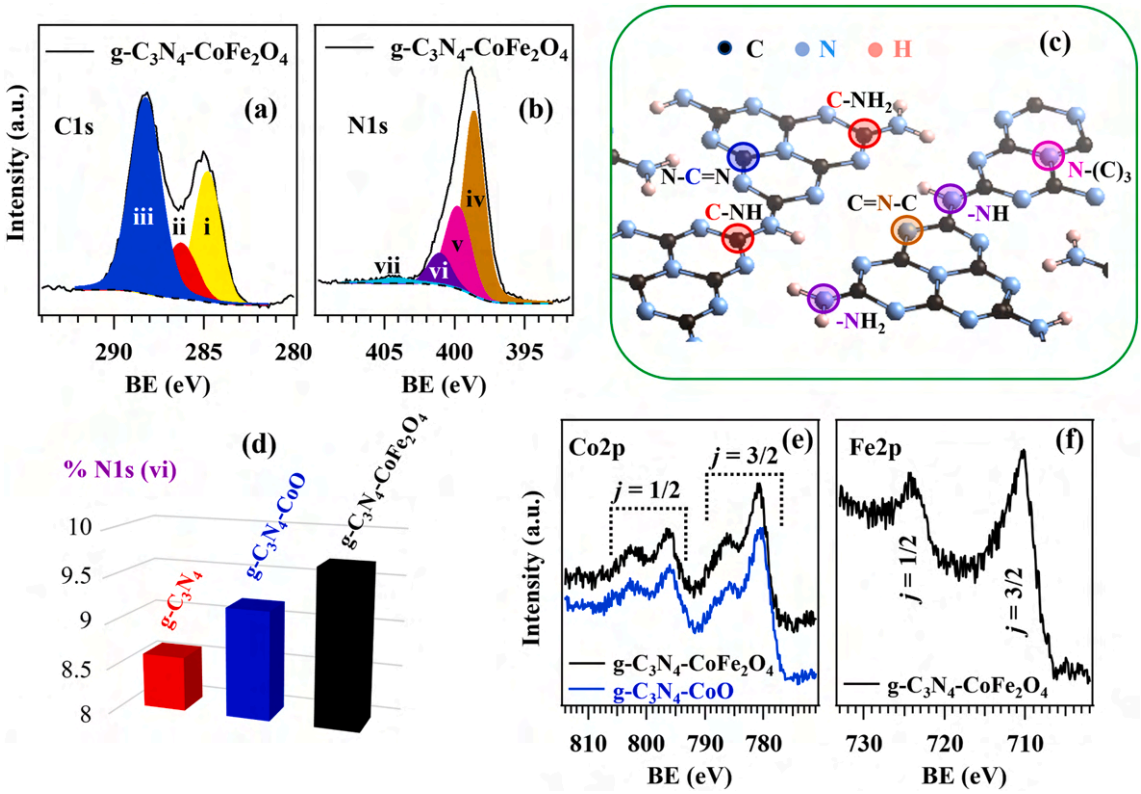

Fig. 2. Surface XPS analysis of carbon nitride-based specimens. (a) C1s and (b) N1s photopeaks for sample g-C_3N_4-$CoFe_2O_4$. (c) Schematic representation of graphitic carbon nitride structure [51], with the indication of non-equivalent carbon and nitrogen atoms. Color codes are the same as in panels (a) and (b). (d) Contribution of the (**vi**) N1s component to the overall N1s signal for the investigated specimens. Co2p (e) and Fe2p (f) photopeaks for g-C_3N_4-CoO and g-C_3N_4-$CoFe_2O_4$ specimens.

($Fe2p_{3/2}$) = 710.6 eV; SOS = 13.3 eV], was in line with that reported for MFe_2O_4 with M = Mg, Co [17,31,33,53,57–58].

Material morphological organization was preliminarily investigated by FE-SEM analyses performed in different sample regions, that enabled to ascertain material lateral homogeneity. Bare g-C_3N_4 (Fig. S5) possessed a granular texture resulting from the assembly of uniformly interconnected grains with a broad dimensional distribution (500 nm – 4 μm; mean deposit thickness = 13 μm), yielding an open area deposit. Functionalized specimens displayed qualitatively similar features (Fig. 3), confirming thus that the adopted RF-sputtering conditions were mild enough to prevent appreciable modifications/alterations of the pristine g-C_3N_4. Nonetheless, a detailed inspection of higher magnification FE-SEM images in Fig. 3 revealed the presence of globular nanoaggregates related to metal oxides deposited *via* RF-sputtering. In-plane elemental maps recorded by EDXS (Fig. S6 and S7) confirmed that, in line with XPS and TEM investigation (see below), CoO or $CoFe_2O_4$ were evenly dispersed on the underlying g-C_3N_4 deposit. In addition, cross-sectional line-scan analyses on functionalized samples (Fig. S8 and S9) pointed out that the presence of functionalizing metal oxides was not limited to the outer regions of carbon nitride deposits, but extended even to the inner ones. This behaviour indicated the occurrence of an intimate contact between g-C_3N_4 and the introduced complementary catalysts, an important issue to exploit their mutual interplay and obtain an enhanced functional activity (see below). Such a result was related to the synergistical combination of the inherent RF-sputtering infiltration power and the open area morphology of the used carbon nitride deposits [12,40].

Since X-ray diffraction (XRD) analyses (Fig. S10 and related observations) did not provide any clear-cut evidence for the presence of CoO or $CoFe_2O_4$, carbon nitride peaks being the only detectable ones, efforts were devoted to an advanced investigation by TEM and related techniques, to better elucidate the system structure and nano-organization. SAED, as well as BF-STEM and HAADF-STEM were used for phase identification, whereas compositional analyses were performed by EDXS and EELS.

For g-C_3N_4-CoO, spherical nanoparticles with average dimensions of (5 ± 1) nm could be observed (Fig. 4a). The pertaining SAED pattern was characterized by rings featuring many diffraction spots, due to the contribution of various randomly oriented nanoparticles within the analyzed area. Comparison of *d*-spaces with data reported for the different cobalt oxides showed the best agreement with cubic CoO [61], which was confirmed to be phase pure by overlaying a simulated diffraction pattern (Fig. 4b). These results were in excellent agreement with XPS ones (see above and Fig. 2). High resolution (HR) HAADF-STEM imaging showed a CoO nanoparticle in [1 1 2] zone axis, in good accordance with the simulation (Fig. 4c, indicated by 'S'). EELS analysis of the Co $L_{2,3}$ edge recorded on the nanoparticles (blue spectrum in Fig. 4d) presented a high similarity with that of a CoO reference [62–63], in line with the results obtained by the analysis of the O *K* edge (Fig. S11).

Analysis of g-C_3N_4-$CoFe_2O_4$ specimen shows crystalline nanoparticles with a mean diameter of (5 ± 1) nm (Fig. 5a). A comparison of the experimental SAED pattern with available ones for known Co-Fe-O phases showed the best agreement with spinel-type $CoFe_2O_4$ [64] (Fig. 5b). The presence of the latter, revealed also by XPS data, was further supported by the good agreement between simulated and experimental HAADF-STEM images shown in Fig. 5c, as well as by a careful comparison with literature data [60,65] of EELS spectra of Co $L_{2,3}$, Fe $L_{2,3}$ (Fig. 5d) and O K (Fig. S13) edges.

In order to evaluate the light-harvesting properties of the prepared samples as OER photoanodes, optical absorption analyses were carried out. The recorded spectra (Fig. 6a) were dominated by a net reflectance decrease at λ < 450 nm, corresponding to interband electronic transitions in carbon nitride [66–68], the predominant system component (see XPS results). In line with this observation, the optical band gap (E_G), obtained from Tauc plots in Fig. 6b, was very similar for all samples (average value = 2.67 eV) [12,16,30,34,39,69]. These outcomes also indicated that no carbon nitride doping, with consequent creation of impurity levels in the band gap, took place under the adopted processing conditions. Nevertheless, a detailed inspection of the recorded optical spectra showed a reflectance decrease (*i.e.*, an absorption increase) in the Vis spectral region upon functionalization of bare g-C_3N_4 samples, especially in the case of g-C_3N_4-$CoFe_2O_4$. This phenomenon, in accordance with previous studies [17,26,34,69], is one of the issues

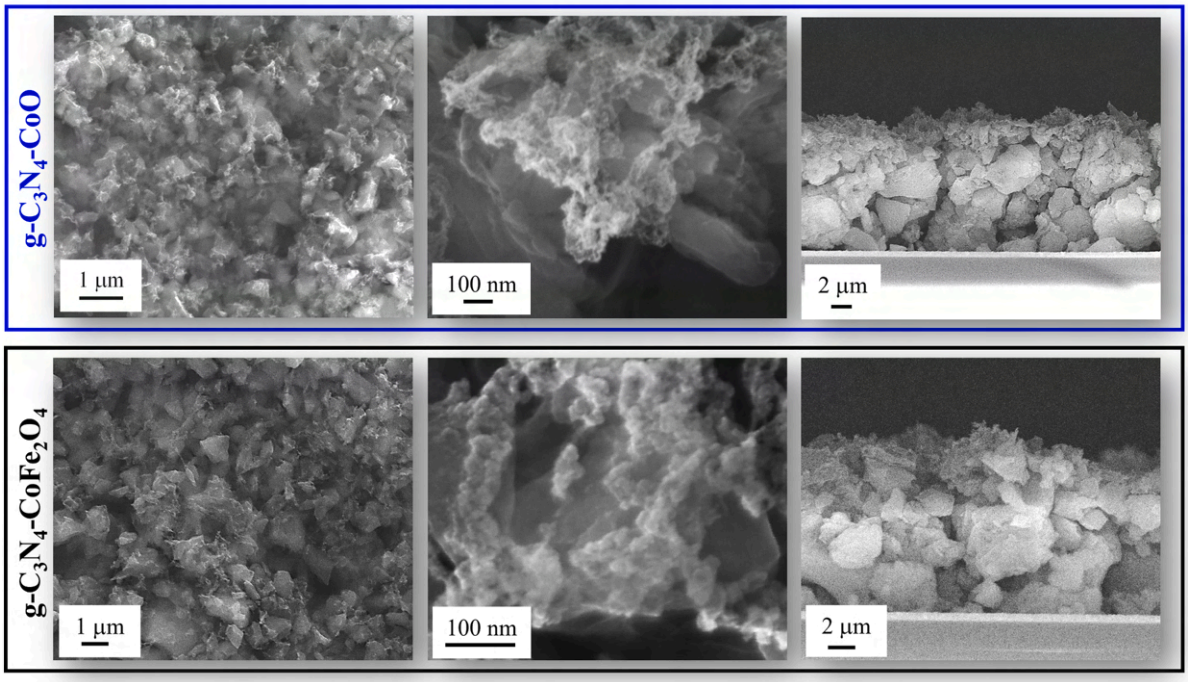

Fig. 3. Plane-view and cross-sectional FE-SEM images of g-C_3N_4-CoO and g-C_3N_4-$CoFe_2O_4$ electrodes.

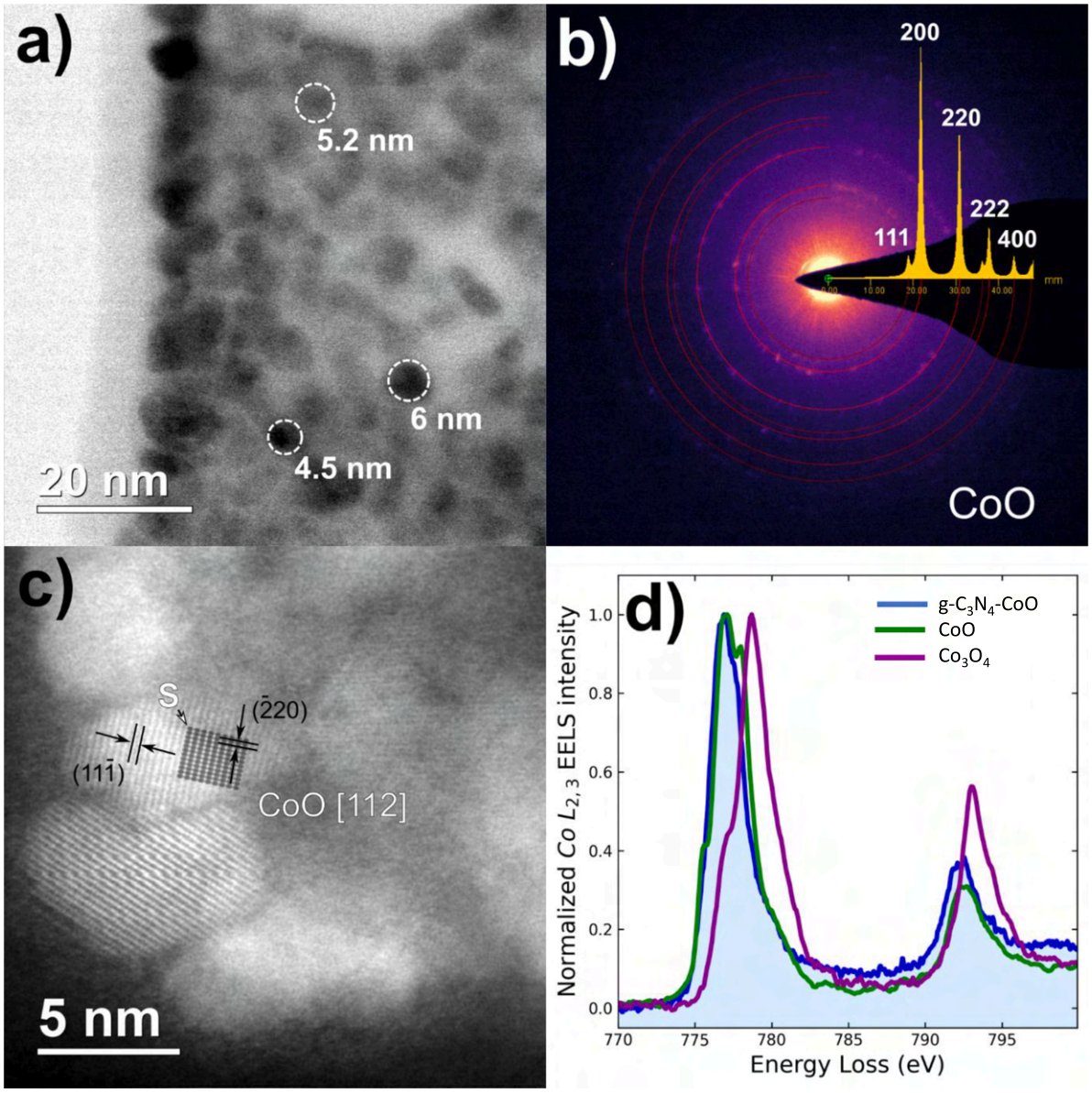

Fig. 4. TEM study of a g-C_3N_4-CoO specimen. a) BF-STEM image. b) Experimental and simulated (overlayed) SAED diffraction pattern showing the presence of the cubic CoO phase. c) Atomic resolution HAADF-STEM image of one CoO nanoparticle in the [1 1 2] zone axis, in good agreement with simulated image ('S'). d) EELS spectra of the Co $L_{2,3}$ edge acquired on the nanoparticle (in blue) compared to reference spectra taken on CoO (green) and Co_3O_4 (purple) powders (see SI and Fig. S12). (For interpretation of the references to color in this figure legend, the reader is referred to the web version of this article.)

accounting for the improved photoactivity of functionalized carbon nitride materials (see below).

3.2. Photoelectrochemical tests

The results of OER functional tests performed on the target systems are presented in Fig. 7 (see also Table S5-S6 and Fig. S14). Chopped light LSV analyses (Fig. 7a) showed good current density values already below the water oxidation thermodynamic potential. The current density values, provided in Table S5-S6, are in line with those reported by other authors for homologous systems (see Table S7). In particular, a comparison of LSV scans reveals a favourable photocurrent density increase upon g-C_3N_4 functionalization with the target complementary catalysts, according to the following sequence: g-C_3N_4 < g-C_3N_4-CoO < g-C_3N_4-$CoFe_2O_4$ (Fig. 7b). This photoactivity order was in perfect agreement with the information gained by ABPE curves (Fig. 7c), showing a favourable shift of the whole profile to lower potential values in comparison to bare g-C_3N_4 and confirming that g-C_3N_4-$CoFe_2O_4$ was the best performing photoanode (see the data in Table S5). Tafel plots acquired in the dark and under illumination (Fig. S14) yielded slope values favourably comparing with analogous catalysts previously reported in the literature, as well as with various benchmark electrode materials based on IrO_2 and RuO_2 (compare the data in Table S6 with the ones in Table S7-S8).

In view of practical applications of the developed systems as OER electrocatalysts, the assessment of material service life is an important issue. In the case of g-C_3N_4-based systems, the stability is known to be directly affected by both the adopted preparation route and the system engineering by combination with other suitable agents [21]. In this work, a preliminar investigation in this regard was accomplished by CA measurements for a total duration of 1 h. The obtained results (Fig. 7d) revealed that for the pristine g-C_3N_4 a current density loss of 36.4 % took place, whereas the presence of functionalizing agents yielded an improved material durability, reducing the observed photocurrent

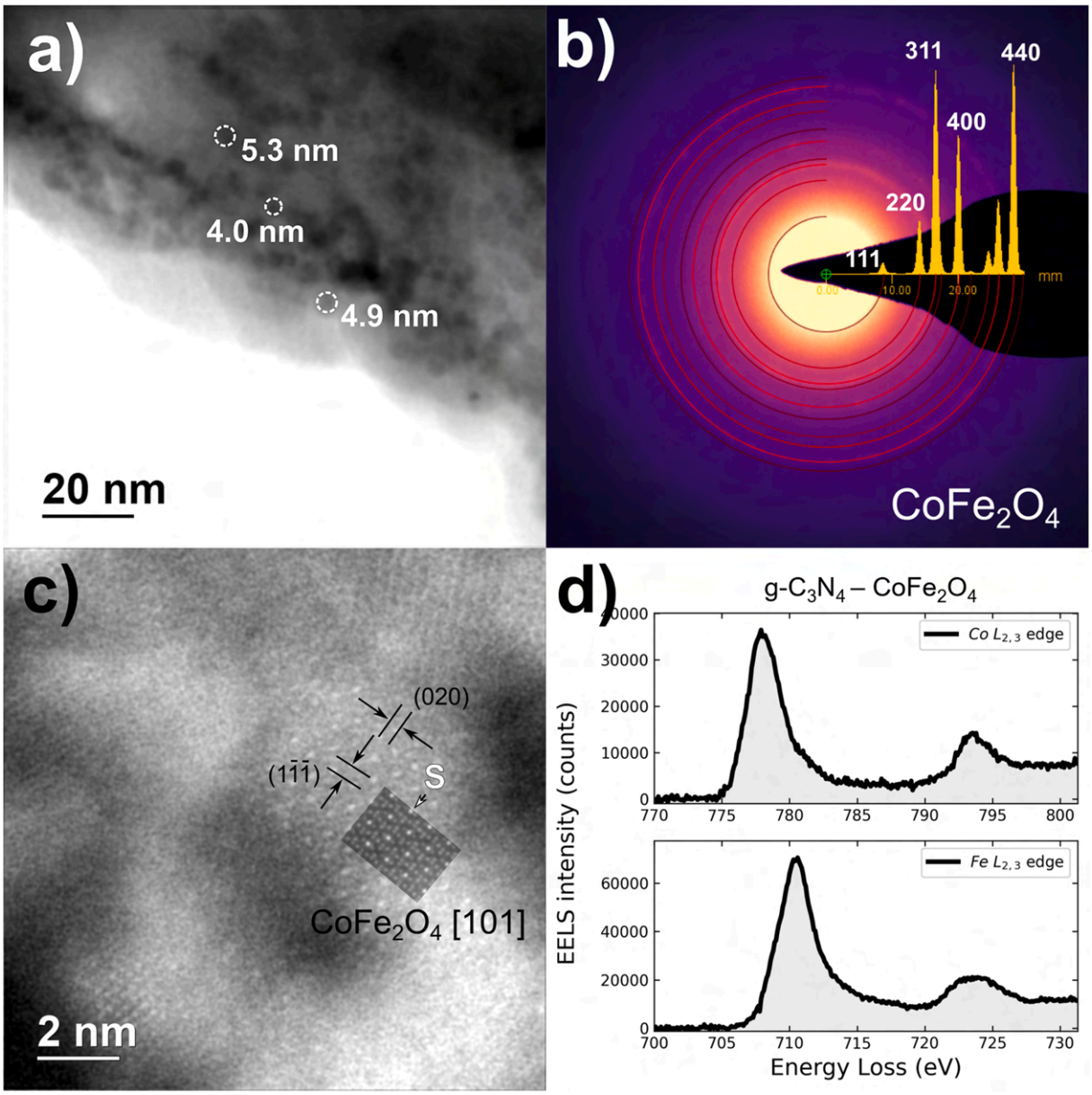

Fig. 5. TEM study of a g-C_3N_4-$CoFe_2O_4$ specimen. a) BF-STEM image. b) Experimental and simulated (overlayed) SAED diffraction pattern showing the occurrence of spinel-type $CoFe_2O_4$. c) Atomic resolution HAADF-STEM image of one $CoFe_2O_4$ nanoparticle in the [1 0 1] zone axis, in good agreement with simulated image ('S'). d) EELS spectra of the Co (top) and Fe (bottom) $L_{2,3}$ edges acquired on the nanoparticle, in agreement with literature [60].

decrease to 9.1 % and 11.3 % for g-C_3N_4-CoO and g-C_3N_4-$CoFe_2O_4$, respectively. These latter variations were lower than those reported for g-C_3N_4-based systems as such [48], incorporated with Co^{2+} [30] or combined with Au and/or Ag [12,70], TiO_2 [46], $MnCo_2O_4$ [71], Co_3O_4 [25], SnO_2 and SnS_2 [72], $Co(OH)_2$ [26], $Ni(OH)_2$ [73], CuTi- and NiFe-layered double hydroxides [45,74], as well as on mixed Co nitride and oxide nanofragments encapsulated in nitrogen-doped carbon nanostructures [75]. In addition, the target materials were stored for six months under ordinary laboratory conditions and tested every 90 days as OER photoanodes. The results revealed the occurrence of very modest photocurrent density variations (Fig. S15), confirming a good operational stability. This conclusion was further validated by XPS analyses performed after long-time operation (see Fig. S16; compare with Fig. 2a, b,e,f and with Fig. S2, S3 and S4) and XRD (Fig. S17; compare with Fig. S10), that allowed to rule out appreciable degradation/dissolution phenomena upon prolonged photoelectrochemical testing. Taken together, these issues underline the applicative potential of the present systems, free from toxic and expensive noble metals and endowed with a very low content of functionalizing agents, towards the development of cost-effective OER electrocatalysts for real-world applications.

The attractive performance improvement resulting by g-C_3N_4 functionalization with low amounts of CoO and $CoFe_2O_4$ can be attributed to the synergistic concurrence of different factors. Beside the enhanced radiation absorption and the increased nitrogen defect content, promoting charge carrier separation (see the above UV–Vis and XPS data), a main contributing effect is due to the close contact between g-C_3N_4 and the introduced functionalizing agents, resulting, in turn, in the efficient formation of junctions boosting electron-hole separation.

A detailed examination of the latter junctions can indeed enable a deeper insight into the underlying mechanism. When a semiconductor is in contact with a solution, the thermal equilibrium established at the interface causes a band bending due to Fermi level (E_F) shifting, and the occurrence of a voltage drop across the space charge layer. The E_F energy position can be determined by measuring the open circuit potential

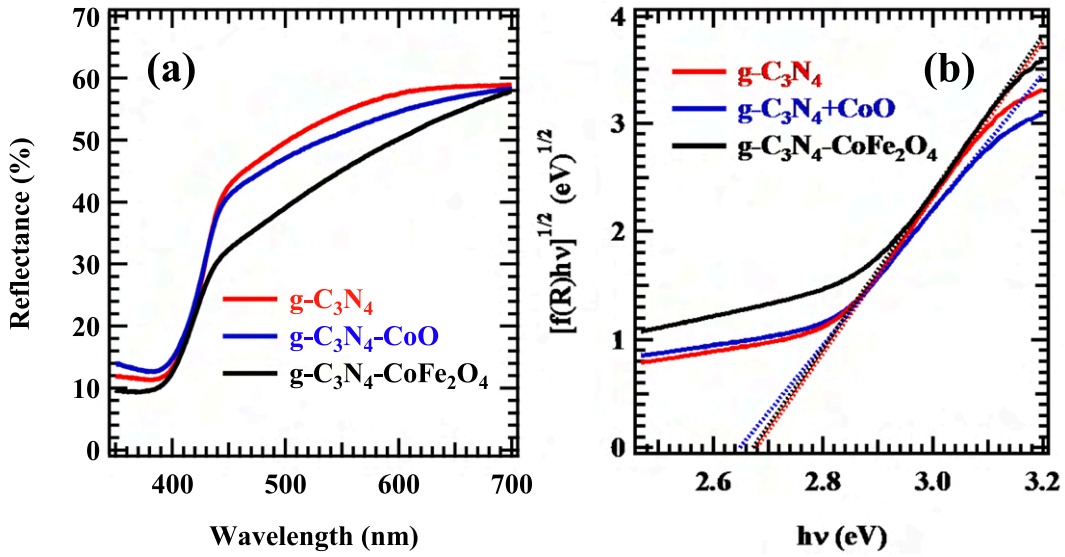

Fig. 6. (a) Diffuse reflectance spectra and (b) Tauc plots for bare and functionalized carbon nitride samples supported on FTO.

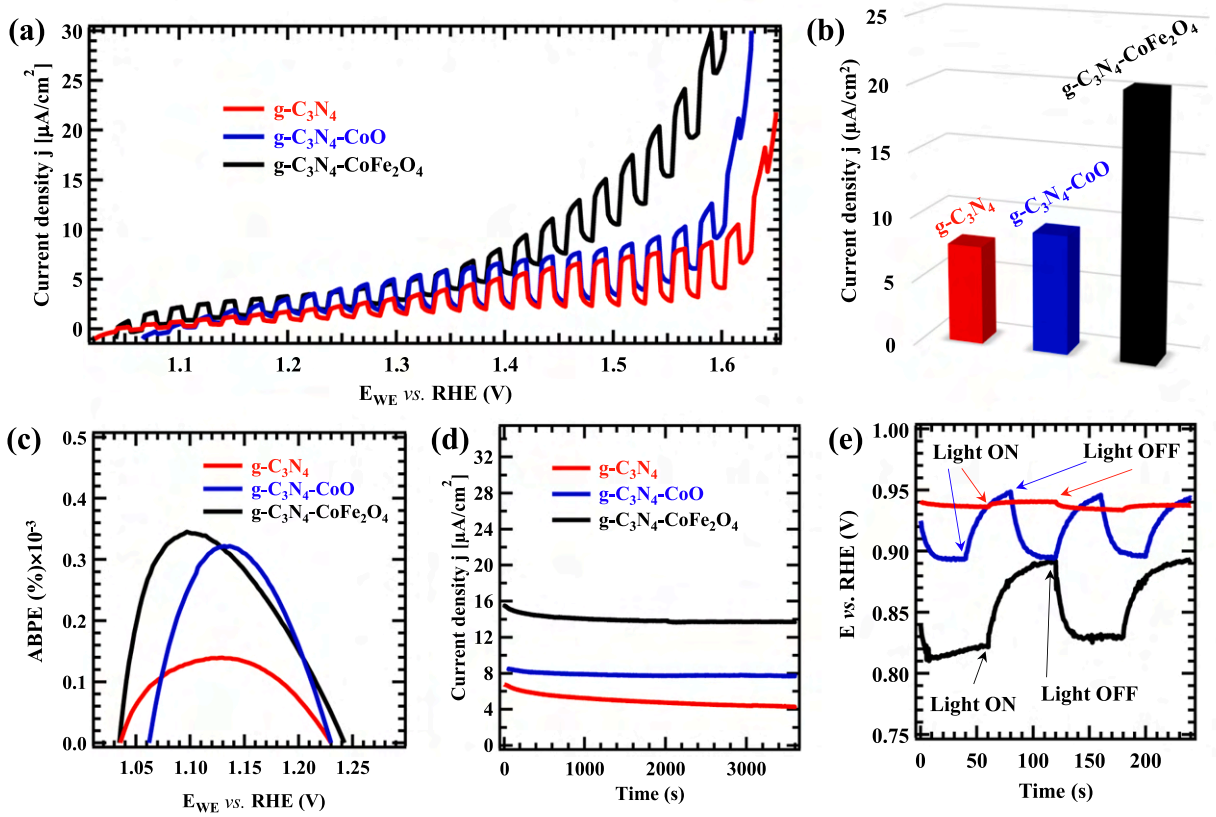

Fig. 7. Photoelectrochemical characterization of bare and functionalized carbon nitride electrodes. (a) Chopped light linear sweep voltammetries. Corresponding photocurrent density values at 1.5 V *vs* RHE (b), ABPE % curves (c), CA curves registered at 1.5 V *vs* RHE (d), and photopotential curves collected at the open circuit potential (OCP) with LED light pulses of 50 mW/cm^2 (e).

(OCP) with respect to the reference electrode [76]. This calculation was performed for all the investigated materials, obtaining a value of ≈ 1.0 V *vs* RHE, which was used as a starting point to build up the schematic diagrams reported in Fig. 8. The difference between E_F and the valence band (VB) edge energies enabled us to set the VB edge position for g-C_3N_4 (VB – E_F ≈ 1.65 eV [77]), CoO (VB – E_F ≈ 0.31 eV [78]), and $CoFe_2O_4$ (VB – E_F ≈ 1.22 eV [77]) on the RHE scale. Basing on the band gap values of g-C_3N_4 (2.67 eV, determined by optical measurements; see above), CoO (2.50 eV [79]), and $CoFe_2O_4$ (1.70 eV [77]), the corresponding conduction band (CB) edge positions can be subsequently derived. It is worthwhile noticing that, for both g-C_3N_4-CoO and g-C_3N_4-$CoFe_2O_4$, experimental results are compatible only with an *n*-type behaviour of the overall electrocatalyst (see also below), in agreement with the fact that graphitic carbon nitride is the predominant system component. This implies that, in the case of g-C_3N_4-CoO, the formation of a *p-n* junction must be considered, since electrons must reach the

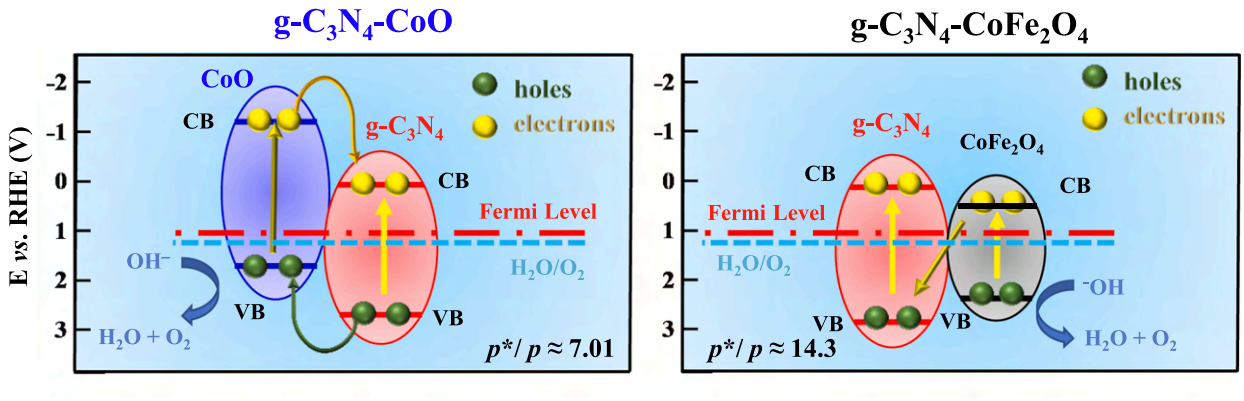

Fig. 8. Approximate representation of the junction between g-C_3N_4 and CoO (left) or $CoFe_2O_4$ (right) [12,77,79]. Despite CoO is known to undergo a progressive transformation into Co_3O_4 upon prolonged air exposure, in the present case, all the performed analytical characterizations revealed the occurrence of phase-pure CoO. As a consequence, Co_3O_4 was not taken into account in the construction of the energy band diagram proposed in this figure.

counterelectrode through g-C_3N_4 flakes, the material in contact with the FTO substrate. In fact, a *Z*-type scheme, leaving electrons in the CoO conduction band, would not account for the system activity.

In a different way, in the case of g-C_3N_4-$CoFe_2O_4$, a *Z*-scheme junction is the only possibility enabling to explain the observed behaviour. The experimental proof for the existence of this *Z*-scheme junction is provided by the increase in the photocurrent density and ABPE values observed upon carbon nitride functionalization (see Fig. 7a-c), and further useful indications are provided by measuring the OCP shift upon illumination. A negative shift in the OCP position indicates an *n*-type behaviour of the investigated material, and a corresponding upward band bending [80]. This behaviour was confirmed for all the investigated specimens, but with important differences. It is worthwhile recalling that the amplitude of the OCP position shift upon illumination corresponds to a photopotential (ΔE_{ph}) which, for an *n*-type semiconductor with a relatively higher impurity concentration ($\geq 10^{17}$ cm^{-3}), can be expressed as [80–81]:

$$\Delta E_{ph} = (K_B T/e) \times ln(p^*/p) \quad (3)$$

where K_B is the Boltzmann constant, T is the absolute temperature (in K), p^* is concentration of holes generated under illumination, whereas p is the corresponding value in the dark. The photopotential curves recorded as a function of time upon intermittent illumination (Fig. 7e) are respectively ≈ 5, 50 and 70 mV for pristine g-C_3N_4, g-C_3N_4-CoO and g-C_3N_4-$CoFe_2O_4$, respectively. These values enable to calculate, using equation (3) at room temperature, the following p^*/p ratios: 1.21, for g-C_3N_4; 7.01, for g-C_3N_4-CoO; 14.3, for g-C_3N_4-$CoFe_2O_4$. The large increase in p^*/p values for g-C_3N_4-CoO and g-C_3N_4-$CoFe_2O_4$ in comparison to bare carbon nitride can be explained by a more efficient separation of photogenerated charge carriers, thanks to the formation of *p-n* or, even better, *Z*-scheme junctions between g-C_3N_4 and the introduced complementary catalysts. The occurrence of these junctions finds its counterpart in higher photocurrent densities in the reported chopped LSVs (see Fig. 7a-b).

4. Conclusions

This study has focused on the functionalization of supported carbon nitride materials with a minimum amount of complementary catalysts capable of boosting the resulting photoelectrochemical activity in the oxygen evolution reaction. Specifically, g-C_3N_4 deposits have been fabricated on FTO substrates by a simple decantation from isopropanol suspensions, followed by functionalization with very low amounts of CoO or $CoFe_2O_4$ nanoparticles by RF-sputtering, and final thermal treatment in an inert atmosphere. The outcomes of a multi-technique investigation revealed, for g-C_3N_4-CoO and g-C_3N_4-$CoFe_2O_4$, the formation of pure materials featuring an intimate contact between the system components, a higher Vis light absorption and an enhanced defect content in comparison to the pristine carbon nitride. Taken together, these features were responsible for an enhanced activity in photoassisted OER processes, especially for g-C_3N_4-$CoFe_2O_4$. The obtained results were rationalized basing on the formation of carbon nitride/oxide heterojunctions, whose nature was directly dependent on the used complementary catalyst, affording an enhanced separation of photogenerated electrons and holes. These characteristics were accompanied by a favorable time stability even in comparison to various previously reported g-C_3N_4-based materials, a feature of remarkable interest for eventual practical end-uses.

Overall, our work demonstrates a simple and potentially scalable methodology for the preparation of carbon nitride photoanodes with improved photoelectrochemical performances by the introduction of functionalizing agents in a very low amount. Indeed, the proposed strategy opens new opportunities for the development of efficient electrocatalysts for clean energy production. Yet, additional efforts will have to be devoted to further refinements of material long-term stability under various operational conditions, and to properly address issues limiting the photon-to-current efficiency, in order to progress towards performances enabling commercial viability. Future work will be also dedicated to the design and development of g-C_3N_4-oxide materials on porous metallic scaffolds, endowed with a large active area and a desirable electrical conductivity, not only as OER photoanodes, but even as electrocatalysts for water purification. The implementation of active functional systems simultaneously enabling energy production and water purification possesses in fact a strategical importance for a future sustainable development.

CRediT authorship contribution statement

Mattia Benedet: Conceptualization, Investigation, Methodology, Data curation, Writing – original draft. **Gian Andrea Rizzi:** Conceptualization, Investigation, Validation, Formal analysis, Writing – original draft, Writing – review & editing. **Alberto Gasparotto:** Funding acquisition, Supervision, Validation, Writing – review & editing. **Nicolas Gauquelin:** Investigation, Methodology, Formal analysis, Writing – review & editing. **Andrey Orekhov:** Investigation, Methodology, Formal analysis, Writing – review & editing. **Johan Verbeeck:** Visualization, Funding acquisition, Writing – review & editing. **Chiara Maccato:** Conceptualization, Supervision, Funding acquisition, Formal analysis, Writing – review & editing. **Davide Barreca:** Conceptualization, Project administration, Funding acquisition, Supervision, Writing – review & editing.

Declaration of Competing Interest

The authors declare that they have no known competing financial interests or personal relationships that could have appeared to influence the work reported in this paper.

Data availability

Data will be made available on request.

Acknowledgements

The authors gratefully acknowledge financial support from CNR (Progetti di Ricerca @CNR – avviso 2020 - ASSIST), Padova University (P-DiSC#04BIRD2020-UNIPD EUREKA, DOR 2020–2022), AMGA Foundation (NYMPHEA project), INSTM Consortium (INSTM21PDGASPAROTTO - NANO^{MAT}, INSTM21PDBARMAC - ATENA) and the European Union's Horizon 2020 research and innovation program under grant agreement No 823717 – ESTEEM3. The FWO-Hercules fund G0H4316N 'Direct electron detector for soft matter TEM' is also acknowledged. Many thanks are due to Prof. Luca Gavioli (Università Cattolica del Sacro Cuore, Brescia, Italy) and Dr. Riccardo Lorenzin (Department of Chemical Sciences, Padova University, Italy) for their invaluable technical support.

Appendix A. Supplementary material

Supplementary data to this article can be found online at https://doi.org/10.1016/j.apsusc.2023.156652.

References

[1] L. Wang, W. Si, Y. Tong, F. Hou, D. Pergolesi, J. Hou, T. Lippert, S.X. Dou, J. Liang, Graphitic carbon nitride (g-C_3N_4)-based nanosized heteroarrays: promising materials for photoelectrochemical water splitting, Carbon Energy 2 (2020) 223–250.

[2] E. Freeman, S. Kumar, V. Celorrio, M.S. Park, J.H. Kim, D.J. Fermin, S. Eslava, Strategies for the deposition of $LaFeO_3$ photocathodes: improving the photocurrent with a polymer template, Sustain. Energy Fuels 4 (2020) 884–894.

[3] M. Regue, S. Sibby, I.Y. Ahmet, D. Friedrich, F.F. Abdi, A.L. Johnson, S. Eslava, TiO_2 photoanodes with exposed {0 1 0} facets grown by aerosol-assisted chemical vapor deposition of a titanium oxo/alkoxy cluster, J. Mater. Chem. A 7 (2019) 19161–19172.

[4] M. Regue, I.Y. Ahmet, P.S. Bassi, A.L. Johnson, S. Fiechter, R. van de Krol, F. F. Abdi, S. Eslava, Zn-doped Fe_2TiO_5 pseudobrookite-based photoanodes grown by aerosol-assisted chemical vapor deposition, ACS Appl. Energy Mater. 3 (2020) 12066–12077.

[5] A. Ali, P.K. Shen, Nonprecious metal's graphene-supported electrocatalysts for hydrogen evolution reaction: Fundamentals to applications, Carbon Energy 2 (2020) 99–121.

[6] L. Schlapbach, A. Züttel, Hydrogen-storage materials for mobile applications, Nature 414 (2001) 353–358.

[7] J. Zhang, Q. Zhang, X. Feng, Support and interface effects in water-splitting electrocatalysts, Adv. Mater. 31 (2019) 1808167.

[8] X. Han, C. Yu, S. Zhou, C. Zhao, H. Huang, J. Yang, Z. Liu, J. Zhao, J. Qiu, Ultrasensitive iron-triggered nanosized Fe–CoOOH integrated with graphene for highly efficient oxygen evolution, Adv. Energy Mater. 7 (2017) 1602148.

[9] M.G. Walter, E.L. Warren, J.R. McKone, S.W. Boettcher, Q. Mi, E.A. Santori, N. S. Lewis, Solar water splitting cells, Chem. Rev. 110 (2010) 6446–6473.

[10] J. Zhang, R. García-Rodríguez, P. Cameron, S. Eslava, Role of cobalt–iron (oxy) hydroxide ($CoFeO_x$) as oxygen evolution catalyst on hematite photoanodes, Energy Environ. Sci. 11 (2018) 2972–2984.

[11] M. Yu, E. Budiyanto, H. Tüysüz, Principles of water electrolysis and recent progress in cobalt-, nickel-, and iron-based oxides for the oxygen evolution reaction, Angew. Chem. Int. Ed. 61 (2022) e202103824.

[12] M. Benedet, G.A. Rizzi, A. Gasparotto, O.I. Lebedev, L. Girardi, C. Maccato, D. Barreca, Tailoring oxygen evolution performances of carbon nitride systems fabricated by electrophoresis through Ag and Au plasma functionalization, Chem. Eng. J. 448 (2022), 137645.

[13] P. Guo, Z. Wang, S. Ge, H. Chen, J. Zhang, H. Wang, S. Liu, S. Wei, X. Lu, In situ coupling reconstruction of cobalt–iron oxide on a cobalt phosphate nanoarray with interfacial electronic features for highly enhanced water oxidation catalysis, ACS Sustainable Chem. Eng. 8 (2020) 4773–4780.

[14] T. Bhowmik, M.K. Kundu, S. Barman, CoFe layered double hydroxide supported on graphitic carbon nitrides: an efficient and durable bifunctional electrocatalyst for oxygen evolution and hydrogen evolution reactions, ACS Appl. Energy Mater. 1 (2018) 1200–1209.

[15] R. Malik, V.K. Tomer, State-of-the-art review of morphological advancements in graphitic carbon nitride (g-CN) for sustainable hydrogen production, Renewable Sustainable Energy Rev. 135 (2021), 110235.

[16] M. Han, H. Wang, S. Zhao, L. Hu, H. Huang, Y. Liu, One-step synthesis of CoO/g-C_3N_4 composites by thermal decomposition for overall water splitting without sacrificial reagents, Inorg. Chem. Front. 4 (2017) 1691–1696.

[17] S. Huang, Y. Xu, M. Xie, H. Xu, M. He, J. Xia, L. Huang, H. Li, Synthesis of magnetic $CoFe_2O_4$/g-C_3N_4 composite and its enhancement of photocatalytic ability under visible-light, Colloids Surf. A 478 (2015) 71–80.

[18] M. Ismael, M. Wark, Photocatalytic activity of $CoFe_2O_4$/g-C_3N_4 nanocomposite toward degradation of different organic pollutants and their inactivity toward hydrogen production: the role of the conduction band position, FlatChem 32 (2022), 100337.

[19] M.I. Chebanenko, L.A. Lebedev, V.L. Ugolkov, N.D. Prasolov, V.N. Nevedomskiy, V. I. Popkov, Chemical and structural changes of g-C_3N_4 through oxidative physical vapor deposition, Appl. Surf. Sci. 600 (2022), 154079.

[20] J. Yang, H. Song, O. Xu, S. Wan, X. Zhu, Preparation of g-C_3N_4@bismuth dihalide oxide heterojunction membrane and its visible light catalytic performance, Appl. Surf. Sci. 583 (2022), 152462.

[21] J. Safaei, N.A. Mohamed, M.F. Mohamad Noh, M.F. Soh, N.A. Ludin, M.A. Ibrahim, W.N. Roslam Wan Isahak, M.A. Mat Teridi, Graphitic carbon nitride (g-C_3N_4) electrodes for energy conversion and storage: a review on photoelectrochemical water splitting, solar cells and supercapacitors, J. Mater. Chem. A 6 (2018) 22346–22380.

[22] H. Che, C. Liu, G. Che, G. Liao, H. Dong, C. Li, N. Song, C. Li, Facile construction of porous intramolecular g-C_3N_4-based donor-acceptor conjugated copolymers as highly efficient photocatalysts for superior H_2 evolution, Nano Energy 67 (2020), 104273.

[23] F. Mei, J. Zhang, C. Liang, K. Dai, Fabrication of novel CoO/porous graphitic carbon nitride S-scheme heterojunction for efficient CO_2 photoreduction, Mater. Lett. 282 (2021), 128722.

[24] M.Z. Rahman, C.B. Mullins, Understanding charge transport in carbon nitride for enhanced photocatalytic solar fuel production, Acc. Chem. Res. 52 (2019) 248–257.

[25] Z. Tian, X. Yang, Y. Chen, H. Huang, J. Hu, B. Wen, Fabrication of alveolate g-C_3N_4 with nitrogen vacancies via cobalt introduction for efficient photocatalytic hydrogen evolution, Int. J. Hydrogen Energy 45 (2020) 24792–24806.

[26] H. Zhang, W. Tian, X. Guo, L. Zhou, H. Sun, M.O. Tadé, S. Wang, Flower-like cobalt hydroxide/oxide on graphitic carbon nitride for visible-light-driven water oxidation, ACS Appl. Mater. Interfaces 8 (2016) 35203–35212.

[27] Z. Zhao, Y. Sun, F. Dong, Graphitic carbon nitride based nanocomposites: a review, Nanoscale 7 (2015) 15–37.

[28] G.A. Rizzi, L. Girardi, Metal oxides for photoelectrochemical fuel production. In Tailored functional oxide nanomaterials: from design to multi-purpose applications, Edited by C. Maccato and D. Barreca, Wiley-VCH: 2022.

[29] L. Liao, Q. Zhang, Z. Su, Z. Zhao, Y. Wang, Y. Li, X. Lu, D. Wei, G. Feng, Q. Yu, X. Cai, J. Zhao, Z. Ren, H. Fang, F. Robles-Hernandez, S. Baldelli, J. Bao, Efficient solar water-splitting using a nanocrystalline CoO photocatalyst, Nat. Nanotechnol. 9 (2014) 69–73.

[30] Z. Chen, H. Wang, J. Xu, J. Liu, Surface engineering of carbon nitride electrode by molecular cobalt species and their photoelectrochemical application, Chem. Asian J. 13 (2018) 1539–1543.

[31] B. Palanivel, M. Lallimathi, B. Arjunkumar, M. Shkir, T. Alshahrani, K.S. Al-Namshah, M.S. Hamdy, S. Shanavas, M. Venkatachalam, G. Ramalingam, rGO supported g-C_3N_4/$CoFe_2O_4$ heterojunction: visible-light-active photocatalyst for effective utilization of H_2O_2 to organic pollutant degradation and OH radicals production, J. Environ. Chem. Eng. 9 (2021), 104698.

[32] B. Rani, A.K. Nayak, N.K. Sahu, Electrochemical supercapacitor application of $CoFe_2O_4$ nanoparticles decorated over graphitic carbon nitride, Diamond Relat. Mater. 120 (2021), 108671.

[33] Ö. Görmez, E. Yakar, B. Gözmen, B. Kayan, A. Khataee, $CoFe_2O_4$ nanoparticles decorated onto graphene oxide and graphitic carbon nitride layers as a separable catalyst for ultrasound-assisted photocatalytic degradation of Bisphenol-A, Chemosphere 288 (2022), 132663.

[34] F. Guo, W. Shi, H. Wang, M. Han, H. Li, H. Huang, Y. Liu, Z. Kang, Facile fabrication of a CoO/g-C_3N_4 *p–n* heterojunction with enhanced photocatalytic activity and stability for tetracycline degradation under visible light, Catal. Sci. Technol. 7 (2017) 3325–3331.

[35] J. Niu, Y. Xie, H. Luo, Q. Wang, Y. Zhang, Y. Wang, Cobalt oxide loaded graphitic carbon nitride as adsorptive photocatalyst for tetracycline removal from aqueous solution, Chemosphere 218 (2019) 169–178.

[36] L. Zhao, D. Yang, L. Ma, X. Feng, H. Ding, An efficient heterogeneous catalyst of $FeCo_2O_4$/g-C_3N_4 composite for catalytic peroxymonosulfate oxidation of organic pollutants under visible light, Colloids Surf., A 610 (2021), 125725.

[37] Q. Song, J. Li, L. Wang, Y. Qin, L. Pang, H. Liu, Stable single-atom cobalt as a strong coupling bridge to promote electron transfer and separation in photoelectrocatalysis, J. Catal. 370 (2019) 176–185.

[38] P.C. Nagajyothi, K. Yoo, I.Y. Eom, J. Shim, $CoFe_2O_4$ NPs supported on graphitic carbon nitride as inexpensive electrocatalysts for methanol oxidation reaction, Ceram. Int. 48 (2022) 11623–11628.

[39] D. Zhang, L. Peng, K. Liu, H. Garcia, C. Sun, L. Dong, Cobalt nanoparticle with tunable size supported on nitrogen-deficient graphitic carbon nitride for efficient visible light driven H_2 evolution reaction, Chem. Eng. J. 381 (2020), 122576.

[40] C. Maccato, L. Bigiani, L. Girardi, A. Gasparotto, O.I. Lebedev, E. Modin, D. Barreca, G.A. Rizzi, Plasma-assisted synthesis of Co_3O_4-based electrocatalysts on Ni foam substrates for the oxygen evolution reaction, Adv. Mater. Interfaces 8 (2021) 2100763.

[41] D. Briggs, M.P. Seah, Practical surface analysis: Auger and X-ray photoelectron spectroscopy, 2nd ed., Wiley, New York, 1990.

[42] https://xpspeak.software.informer.com/4.1/.

[43] Z. Chen, T.F. Jaramillo, T.G. Deutsch, A. Kleiman-Shwarsctein, A.J. Forman, N. Gaillard, R. Garland, K. Takanabe, C. Heske, M. Sunkara, E.W. McFarland, K. Domen, E.L. Miller, J.A. Turner, H.N. Dinh, Accelerating materials development for photoelectrochemical hydrogen production: standards for methods, definitions, and reporting protocols, J. Mater. Res. 25 (2010) 3–16.

[44] T.S. Miller, A.B. Jorge, T.M. Suter, A. Sella, F. Corà, P.F. McMillan, Carbon nitrides: synthesis and characterization of a new class of functional materials, Phys. Chem. Chem. Phys. 19 (2017) 15613–15638.

[45] Y. Hou, Z. Wen, S. Cui, X. Feng, J. Chen, Strongly coupled ternary hybrid aerogels of N-deficient porous graphitic-C_3N_4 nanosheets/N-doped graphene/NiFe-layered double hydroxide for solar-driven photoelectrochemical water oxidation, Nano Lett. 16 (2016) 2268–2277.

[46] J. Wang, W.-D. Zhang, Modification of TiO_2 nanorod arrays by graphite-like C_3N_4 with high visible light photoelectrochemical activity, Electrochim. Acta 71 (2012) 10–16.

[47] K. Wang, Q. Li, B. Liu, B. Cheng, W. Ho, J. Yu, Sulfur-doped g-C_3N_4 with enhanced photocatalytic CO_2-reduction performance, Appl. Catal., B 176-177 (2015) 44–52.

[48] M. Sima, E. Vasile, A. Sima, N. Preda, C. Logofatu, Graphitic carbon nitride based photoanodes prepared by spray coating method, Int. J. Hydrogen Energy 44 (2019) 24430–24440.

[49] H. Yu, R. Shi, Y. Zhao, T. Bian, Y. Zhao, C. Zhou, G.I.N. Waterhouse, L.-Z. Wu, C.-H. Tung, T. Zhang, Alkali-assisted synthesis of nitrogen deficient graphitic carbon nitride with tunable band structures for efficient visible-light-driven hydrogen evolution, Adv. Mater. 29 (2017) 1605148.

[50] J. Fu, B. Zhu, C. Jiang, B. Cheng, W. You, J. Yu, Hierarchical porous O-doped g-C_3N_4 with enhanced photocatalytic CO_2 reduction activity, Small 13 (2017) 1603938.

[51] P. Niu, L.-C. Yin, Y.-Q. Yang, G. Liu, H.-M. Cheng, Increasing the visible light absorption of graphitic carbon nitride (melon) photocatalysts by homogeneous self-modification with nitrogen vacancies, Adv. Mater. 26 (2014) 8046–8052.

[52] Q. Liang, Z. Li, Z.-H. Huang, F. Kang, Q.-H. Yang, Holey graphitic carbon nitride nanosheets with carbon vacancies for highly improved photocatalytic hydrogen production, Adv. Funct. Mater. 25 (2015) 6885–6892.

[53] F. Hu, W. Luo, C. Liu, H. Dai, X. Xu, Q. Yue, L. Xu, G. Xu, Y. Jian, X. Peng, Fabrication of graphitic carbon nitride functionalized P-$CoFe_2O_4$ for the removal of tetracycline under visible light: optimization, degradation pathways and mechanism evaluation, Chemosphere 274 (2021), 129783.

[54] Y. He, J. Huang, B. Wang, Y. Qu, Construction of Z-scheme heterojunction C_3N_4/N-CQDs@$W_{18}O_{49}$ for full-spectrum photocatalytic organic pollutant degradation, Appl. Surf. Sci. 610 (2023), 155255.

[55] Q. Zheng, Y. Xu, Y. Wan, J. Wu, X. Hu, X. Yao, Synthesis of $CoFe_2O_4$-modified g-C_3N_4 with enhanced photocatalytic performance for nitrogen fixation, J. Nanopart. Res. 22 (2020) 301.

[56] Y. Xiao, G. Tian, W. Li, Y. Xie, B. Jiang, C. Tian, D. Zhao, H. Fu, Molecule self-assembly synthesis of porous few-layer carbon nitride for highly efficient photoredox catalysis, J. Am. Chem. Soc. 141 (2019) 2508–2515.

[57] J. Chen, D. Zhao, Z. Diao, M. Wang, S. Shen, Ferrites boosting photocatalytic hydrogen evolution over graphitic carbon nitride: a case study of (Co, Ni)Fe_2O_4 modification, Sci. Bull. 61 (2016) 292–301.

[58] G. Wang, Y. Ma, Z. Wei, M. Qi, Development of multifunctional cobalt ferrite/graphene oxide nanocomposites for magnetic resonance imaging and controlled drug delivery, Chem. Eng. J. 289 (2016) 150–160.

[59] F. Urbain, R. Du, P. Tang, V. Smirnov, T. Andreu, F. Finger, N. Jimenez Divins, J. Llorca, J. Arbiol, A. Cabot, J.R. Morante, Upscaling high activity oxygen evolution catalysts based on $CoFe_2O_4$ nanoparticles supported on nickel foam for power-to-gas electrochemical conversion with energy efficiencies above 80%, Appl. Catal., B 259 (2019), 118055.

[60] N. Daffé, F. Choueikani, S. Neveu, M.-A. Arrio, A. Juhin, P. Ohresser, V. Dupuis, P. Sainctavit, Magnetic anisotropies and cationic distribution in $CoFe_2O_4$ nanoparticles prepared by co-precipitation route: influence of particle size and stoichiometry, J. Magn. Magn. Mater. 460 (2018) 243–252.

[61] H.N. Ok, J.G. Mullen, Evidence of two forms of cobaltous oxide, Phys. Rev. 168 (1968) 550–562.

[62] Y.-J. Zeng, N. Gauquelin, D.-Y. Li, S.-C. Ruan, H.-P. He, R. Egoavil, Z.-Z. Ye, J. Verbeeck, J. Hadermann, M.J. Van Bael, C. Van Haesendonck, Co-rich ZnCoO nanoparticles embedded in wurtzite $Zn_{1-x}Co_xO$ thin films: possible origin of superconductivity, ACS Appl. Mater. Interfaces 7 (2015) 22166–22171.

[63] R. Egoavil, S. Hühn, M. Jungbauer, N. Gauquelin, A. Béché, G. Van Tendeloo, J. Verbeeck, V. Moshnyaga, Phase problem in the B-site ordering of La_2CoMnO_6: impact on structure and magnetism, Nanoscale 7 (2015) 9835–9843.

[64] T.A.S. Ferreira, J.C. Waerenborgh, M.H.R.M. Mendonça, M.R. Nunes, F.M. Costa, Structural and morphological characterization of $FeCo_2O_4$ and $CoFe_2O_4$ spinels prepared by a coprecipitation method, Solid State Sci. 5 (2003) 383–392.

[65] J.P. Singh, J.Y. Park, V. Singh, S.H. Kim, W.C. Lim, H. Kumar, Y.H. Kim, S. Lee, K. H. Chae, Correlating the size and cation inversion factor in context of magnetic and optical behavior of $CoFe_2O_4$ nanoparticles, RSC Adv. 10 (2020) 21259–21269.

[66] Y. Yu, S. Wu, J. Gu, R. Liu, Z. Wang, H. Chen, F. Jiang, Visible-light photocatalytic degradation of bisphenol A using cobalt-to-oxygen doped graphitic carbon nitride with nitrogen vacancies via metal-to-ligand charge transfer, J. Hazard. Mater. 384 (2020), 121247.

[67] G. Zhang, S. Zang, X. Wang, Layered $Co(OH)_2$ deposited polymeric carbon nitrides for photocatalytic water oxidation, ACS Catal. 5 (2015) 941–947.

[68] S. Xiong, X. Liu, X. Zhu, G. Liang, Z. Jiang, B. Cui, J. Bai, One-step preparation of well-dispersed spindle-like Fe_2O_3 nanoparticles on g-C_3N_4 as highly efficient photocatalysts, Ecotoxicol. Environ. Saf. 208 (2021), 111519.

[69] A. Hassani, P. Eghbali, A. Ekicibil, Ö. Metin, Monodisperse cobalt ferrite nanoparticles assembled on mesoporous graphitic carbon nitride ($CoFe_2O_4$/mpg-C_3N_4): a magnetically recoverable nanocomposite for the photocatalytic degradation of organic dyes, J. Magn. Magn. Mater. 456 (2018) 400–412.

[70] H. Wang, T. Sun, L. Chang, P. Nie, X. Zhang, C. Zhao, X. Xue, The g-C_3N_4 nanosheets decorated by plasmonic Au nanoparticles: A heterogeneous electrocatalyst for oxygen evolution reaction enhanced by sunlight illumination, Electrochim. Acta 303 (2019) 110–117.

[71] A. Rebekah, H. Amir, C. Viswanathan, N. Ponpandian, Enhanced bifunctional aspects of oxygen vacancy rich cation substituted $MnCo_2O_4$ intercalated with g-C_3N_4 as an oxygen evolution and supercapacitor electrode, Int. J. Hydrogen Energy 48 (2023) 6384–6398.

[72] B. Zhang, J. Li, Q. Song, S. Lv, Y. Shi, H. Liu, g-C_3N_4-modulated bifunctional SnO_2@g-C_3N_4@SnS_2 hollow nanospheres for efficient electrochemical overall water splitting, Appl. Surf. Sci. 589 (2022), 153016.

[73] T. Li, X. Ma, J. Wu, F. Chu, L. Qiao, Y. Song, M. Wu, J. Lin, L. Peng, Z. Chen, Ni $(OH)_2$ microspheres in situ self-grown on ultra-thin layered g-C_3N_4 as a heterojunction electrocatalyst for oxygen evolution reaction, Electrochim. Acta 400 (2021), 139473.

[74] S. Guru, S. Kumar, S. Bellamkonda, R.R. Gangavarapu, Synthesis of CuTi-LDH supported on g-C_3N_4 for electrochemical and photoelectrochemical oxygen evolution reactions, Int. J. Hydrogen Energy 46 (2021) 16414–16430.

[75] K.J. Lee, D.Y. Shin, A. Byeon, A. Lim, Y.S. Jo, A. Begley, D.-H. Lim, Y.-E. Sung, H. S. Park, K.H. Chae, S.W. Nam, K.-Y. Lee, J.Y. Kim, Hierarchical cobalt–nitride and –oxide co-doped porous carbon nanostructures for highly efficient and durable bifunctional oxygen reaction electrocatalysts, Nanoscale 9 (2017) 15846–15855.

[76] A.J. Bard, L.R. Faulkner, Electrochemical methods: fundamentals and applications, 2nd Ed., J. Wiley & Sons, Inc., 2000.

[77] M.F. Ehsan, A. Fazal, S. Hamid, M. Arfan, I. Khan, M. Usman, A. Shafiee, M. N. Ashiq, $CoFe_2O_4$ decorated g-C_3N_4 nanosheets: new insights into superoxide anion mediated photomineralization of methylene blue, J. Environ. Chem. Eng. 8 (2020), 104556.

[78] G. Velegraki, I. Vamvasakis, I.T. Papadas, S. Tsatsos, A. Pournara, M.J. Manos, S. A. Choulis, S. Kennou, G. Kopidakis, G.S. Armatas, Boosting photochemical activity by Ni doping of mesoporous CoO nanoparticle assemblies, Inorg. Chem. Front. 6 (2019) 765–774.

[79] K.-W. Park, A.M. Kolpak, Mechanism for spontaneous oxygen and hydrogen evolution reactions on CoO nanoparticles, J. Mater. Chem. A 7 (2019) 6708–6719.

[80] N. Sato, Electrochemistry at metal and semiconductor electrodes, 1st Ed., Elsevier, 1998.

[81] X. Ma, J. Zhang, B. Wang, Q. Li, S. Chu, Hierarchical Cu_2O foam/g-C_3N_4 photocathode for photoelectrochemical hydrogen production, Appl. Surf. Sci. 427 (2018) 907–916.